Characterization of Fe-Based Amorphous Powder Synthesized via Mechanical Alloying and Consecutive Consolidation via Spark Plasma Sintering

M.Tech. Thesis

By

AKASH KUMAR

DEPARTMENT OF METALLURGICAL ENGINEERING AND MATERIALS SCIENCE

INDIAN INSTITUTE OF TECHNOLOGY INDORE

May 2025

Characterization of Fe-Based Amorphous Powder Synthesized via Mechanical Alloying and Consecutive Consolidation via Spark Plasma Sintering

A THESIS

Submitted in the partial fulfilment of the
Requirements for the award of the degree
of

Master of Technology

By

AKASH KUMAR

DEPARTMENT OF METALLURGICAL ENGINEERING AND MATERIALS SCIENCE

INDIAN INSTITUTE OF TECHNOLOGY INDORE

May 2025

INDIAN INSTITUTE OF TECHNOLOGY INDORE

CANDIDATE'S DECLARATION

I hereby certify that the work which is being presented in the thesis entitled **Characterization of Fe-Based Amorphous Powder Synthesized via Mechanical Alloying and Consecutive Consolidation via Spark Plasma Sintering** in the partial fulfillment of the requirements for the award of the degree of **MASTER OF TECHNOLOGY** and submitted in the **DEPARTMENT OF METALLURGICAL ENGINEERING AND MATERIAL SCIENCE, Indian Institute of Technology Indore,** is an authentic record of my work carried out during the period from July 2023 to May 2025 under the supervision of Dr. Ram Sajeevan Maurya, Assistant Professor, Indian Institute of Technology, Indore.

The matter presented in this thesis has not been submitted by me for the award of any other degree of this or any other institute.

Akash Kumar
29/05/2025

Signature of the student with date

Akash Kumar

This is to certify that the above statement made by the candidate is correct to the best of my/our knowledge.

RSM 29/05/2025

Signature of the Supervisor with date

Dr. Ram Sajeevan Maurya

Akash Kumar has successfully given his/her M.Tech. Oral Examination held on **26/05/2025.**

RSM 29/05/2025

Dr. Ram Sajeevan Maurya

Asst. Professor, IIT Indore

Date:

29/05/2025 Acting DPGC

Convener, DPGC

Dept. of MEMS

Date:

ACKNOWLEDGEMENT

I would like to express my heartfelt gratitude and appreciation to the following individuals and organizations who have played a significant role in the successful completion of my M.Tech. thesis:

First and foremost, I am deeply grateful to my research supervisor, **Dr. R.S. Maurya,** for his invaluable guidance, unwavering support, and expert insights throughout the entire research process. His encouragement, patience, and exceptional mentoring have been instrumental in shaping this thesis.

I am thankful to **Dr. Ajay Kushwaha,** HOD MEMS, for his support and cooperation. I am thankful to all the faculty members of the department of MEMS for their guidance and support.

I thank my colleague, Mr. Deepak Kumar Srivastava, for the knowledge transfer on all the instruments I used to complete the experiment.

I would like to acknowledge the support of the staff and technicians of the MEMS Department, IIT Indore, whose valuable assistance, technical expertise, and access to laboratory resources greatly contributed to the successful execution of my research work.

I would like to express my gratitude to **MHRD, Govt of India** for providing fellowship during my master's studies to carry out this research. Their investment has been instrumental in the successful completion of this thesis.

Finally, I would like to thank all the authors, researchers, and scholars whose work and publications have served as a guiding light for my research. Their contributions have laid the foundation for my understanding of the subject matter.

The completion of this M.Tech thesis would not have been possible without the support, guidance, and contributions of the individuals and organizations mentioned above. I am deeply grateful for their involvement and dedication.

DEDICATION

This thesis is dedicated to my
parents, sisters, seniors and friends
for their constant love,
encouragement and patience.

ABSTRACT

This thesis presents a comprehensive study on the synthesis, consolidation, and characterization of Fe-based amorphous alloy powders developed through MA and subsequently consolidated using SPS. Two ternary compositions $Fe_{83.453}Al_{14.560}Ti_{1.987}$ and $Fe_{69.815}Al_{26.860}Ti_{3.325}$ were selected based on their potential glass-forming ability and phase stability. The MA process, carried out for up to 80 hours, led to significant structural refinement and partial amorphization, as confirmed by X-ray diffraction (XRD), transmission electron microscopy (TEM), and selected area electron diffraction (SAED). Scanning electron microscopy (SEM) coupled with energy-dispersive X-ray spectroscopy (EDS) showed morphological evolution and compositional homogeneity with increased milling duration. Particle size analysis indicated a trend of particle refinement followed by agglomeration due to cold welding. Differential scanning calorimetry (DSC) highlighted distinct thermal transformation behaviors for both compositions. Subsequent SPS consolidation at temperatures ranging from 300 °C to 1200 °C resulted in improved densification, with $Fe_{83.453}Al_{14.560}Ti_{1.987}$ exhibiting higher practical density and lower porosity. The XRD patterns of sintered samples revealed the formation of intermetallic phases at elevated temperatures, while SEM analysis demonstrated enhanced inter-particle bonding. Mechanical characterization using the Vickers hardness test showed a substantial increase in hardness with sintering temperature, with a maximum value of 1029 ± 8.7 HV for the $Fe_{83.453}Al_{14.560}Ti_{1.987}$ sample sintered at 1200 °C. The results establish the effectiveness of combining MA and SPS to fabricate high-density Fe-based amorphous alloys with promising structural and functional properties.

TABLE OF CONTENTS

LIST OF FIGURES

LIST OF TABLES

ACRONYMS

SPS – Spark Plasma Sintering

GFA - Glass Forming Ability

XRD – X-ray Diffraction

SEM – Scanning Electron Microscopy

DSC – Differential Scanning Calorimetry

MA – Mechanical Alloying

EDS – Energy Dispersive Spectroscopy

HRTEM – High-Resolution Transmission Electron Microscopy

PCA – Process Control Agent

BPR – Ball-to-powder ratio

Chapter 1

Introduction

1.1 Background

Amorphous alloys, or metallic glasses are class of materials with no long-range crystalline order, typically fabricated by rapid solidification or solid-state processing techniques. This disorder in atomic structure imparts abnormal physical and mechanical properties such as high strength, favorable wear and corrosion resistance, and excellent soft magnetic behavior[1].

Among the different types, Fe-based amorphous alloys are especially important because they possess low cost, rich raw material resources, and good soft magnetic properties, making them ideal for applications in transformers, inductors, and magnetic shielding. Their high strength and hardness also render them appealing for structural applications. Still, processing and synthesizing these materials without causing crystallization is a major challenge, which requires sophisticated methods such as MA and SPS for controlled production[2].

Conventional processing methods such as casting and melt spinning often fall short in producing fully amorphous bulk materials due to their inherent limitations in cooling rates and compositional control. These techniques typically require extremely high quenching rates in the order of 10^5–10^6 K/s to suppress crystallization, which restricts the size and geometry of the resulting amorphous components[3]. Furthermore, maintaining structural homogeneity and avoiding defects during bulk consolidation is challenging with traditional sintering or hot pressing, often leading to grain growth and partial crystallization. These drawbacks have driven the development of alternative solid-state synthesis and densification techniques. MA is a high-energy ball milling process, facilitates the creation of amorphous phase through successive cold wielding and fracturing under room conditions, thus avoiding rapid cooling. Moreover, SPS provides fast consolidation with sharp temperature and time control, reducing crystallization to high-density compacts. In combination,

these methods offer a promising approach to fabricating bulk amorphous materials with predefined properties[4].

1.2 Amorphous Alloys

Amorphous alloys are metallic materials distinguished by their lack of a regular, repeating atomic structure, which sets them apart from traditional crystalline metals. This non-crystalline structure is typically achieved by rapid cooling or mechanical processing methods that inhibit the formation of crystals. Due to this disordered atomic arrangement, amorphous alloys exhibit several remarkable properties, such as high tensile strength, exceptional hardness and superior resistance to corrosion and wear. They also demonstrate unique magnetic behaviors, including low coercivity and high permeability, which are beneficial in electrical and electronic applications. Unlike their crystalline counterparts, amorphous alloys do not have grain boundaries, reducing common failure mechanisms and enabling improved mechanical performance and durability[5].

1.2.1 Formation mechanisms of amorphous materials

Amorphous structures form when atoms are prevented from arranging into a regular crystal lattice, usually by rapid cooling or mechanical alloying. These processes limit atomic movement, causing atoms to “freeze” in a disordered state. The resulting material lacks long-range order but retains short-range atomic arrangements. Factors like alloy composition and processing conditions influence the formation and stability of the amorphous phase[6].

1.2.2 Advantage over crystalline materials and applications in various industries

Amorphous alloys offer several advantages over their crystalline counterparts, including higher strength and hardness, improved corrosion and wear resistance, and superior magnetic properties due to the absence of grain boundaries. These unique features make them ideal for applications in diverse industries such as electronics, where they are used in soft magnetic cores; aerospace and automotive sectors, for lightweight and durable structural components; and biomedical fields, owing to their excellent biocompatibility

and corrosion resistance. Their ability to combine mechanical robustness with functional performance continues to drive research and industrial adoption[7].

1.3 Mechanical Alloying

1.3.1 Principle and process

We use mechanical alloying (MA) in this research as a solid-state synthesis process to create amorphous alloy powders. MA is the solid-state alloying process where cold welding, fracture, and rewelding of the powder particles recur repeatedly throughout the milling duration. It appears to be an easy process, but it has many variables that influence the ultimate quality of the product.

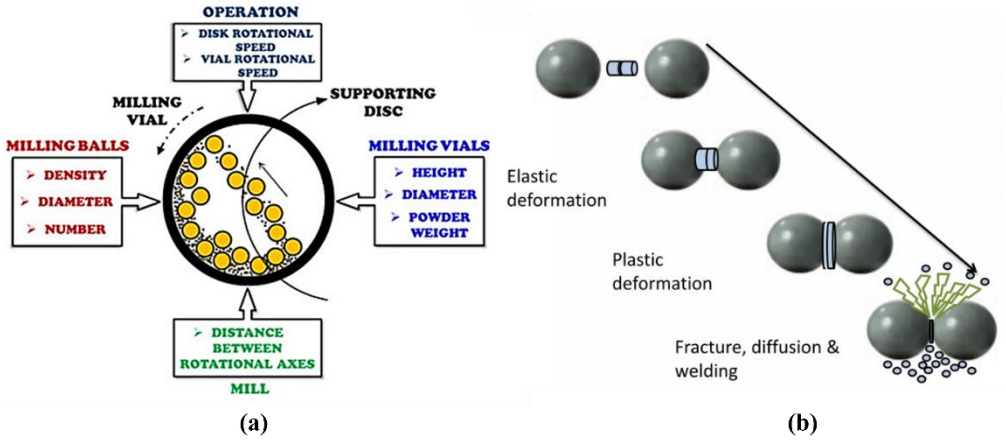

Figure 1.1 (a) Schematic of Ball Milling Process in Planetary Ball Mill (b) collision of balls and powder mixture during Mechanical alloying

The milling parameters include:

- Ball mill type
- Material of the container or vial
- Speed and time of milling
- Grinding medium (wet or dry)
- Ball-to-powder ratio (BPR)
- Size of the balls
- Process control agent (PCA)

During ball milling, powders are blended in necessary amounts in a vial, followed by adding grinding media such as steel balls into the same vial. Subsequently, the powders are milled for a specific period of time to achieve a uniform composition[8].

1.3.2 Key Parameters Affecting Mechanical Alloying

- **Type of Mill:** The choice of mill depends on the material to be milled and the desired characteristics of the final powder. For large-scale powder production, attritor mills or planetary ball mills (e.g., Fritsch Pulverisette) are preferred[8]. These mills operate in a closed chamber with milling balls, typically around 250 rpm. Attritors are significantly faster and more efficient compared to conventional ball mills.
- **Milling Container:** The container material should minimize wear and contamination caused by the repeated impact of the grinding balls. Common materials include hardened steel, tungsten carbide, tool steel, and bearing steel[8].
- **Milling Speed:** Higher milling speeds increase the kinetic energy transferred to the powder, raising the temperature within the vial and improving homogenization of the alloying elements.
- **Milling Duration:** Prolonged milling reduces particle size and enhances alloying. However, longer durations may lead to contamination or formation of unwanted phases[9].
- **Ball Size:** Larger grinding balls impart higher impact energy to the powder particles. Using balls and containers made from the same material minimizes contamination[10].
- **Ball-to-Powder Weight Ratio (BPR):** BPR is a significant determinant of the milling process's efficiency. Values between 1:1 to 220:1 have been investigated. For small mills, it is common to have a 10:1 ratio, while larger mills utilize 50:1 or greater. Higher BPR increases collision frequency, shortens processing time, and enhances energy transfer to the powder[11].
- **Extent of Vial Filling:** For effective milling, the vial should not be filled more than 50% of its volume. Underfilling leads to low production

efficiency, while overfilling reduces the space available for effective collisions between balls and powder.

- **Milling Atmosphere:** To prevent oxidation or contamination, inert gases like high-purity argon or nitrogen are commonly used. Reactive materials like titanium may require tailored atmospheres. Specific environments can be employed to synthesize special alloys or compounds, such as nitrides (using nitrogen or ammonia) and hydrides (using hydrogen)[12].
- **Process Control Agents (PCA):** Ductile powders tend to cold-weld during milling, which hinders alloy formation. To counteract this, 1–5 wt.% PCA is added. PCAs can be in solid, liquid, or gaseous form and generally act by adsorbing particle surfaces to reduce surface energy. Commonly used PCAs include stearic acid, methanol, ethanol and hexane. These agents decompose during milling and may form dispersoid compounds that get embedded in the powder structure[13].

1.4 Spark Plasma Sintering (SPS)

SPS is an advanced powder consolidation method that simultaneously utilizes uniaxial pressure and pulsed direct electric current. The combination facilitates quick sintering of materials at relatively lower temperatures and shorter duration than the normal sintering processes. The efficiency of SPS stems from localized heating induced by the electric current at particle contacts, leading to swift densification with minimal grain growth. Consequently, SPS is particularly effective for consolidating nanostructured and amorphous powders, allowing for the preservation of their unique microstructures and, in turn, enhancing their mechanical properties[14].

1.4.1 Principle and Process

SPS is a process of powder consolidation that utilizes uniaxial pressure and pulsed direct current to compact powders obtained from mechanical alloying. SPS primarily consists of three main stages:

a) **Plasma heating:** In this stage, electrical discharge among the powder particles causes their surfaces to be heated to very high temperatures (a few thousand degrees Celsius). The heat generated is evenly distributed on the

particle surface, leading to the evaporation of impurities and the melting of particles, which facilitate neck formation[15].

b) **Joule heating:** This warming is caused by the electric current, as pulsed DC current flows from particle to particle through the connecting necks. This enhances diffusion, leading to the growth of particles. The localized heating and uniform heat distribution allow for a rapid increase and decrease in temperature, which effectively minimizes grain coarsening[16].

c) **Plastic deformation:** The hot compacts soften and plastically deform when subjected to uniaxial stress, resulting in the formation of densely compacted pellets.

SPS is generally performed using graphite dies. The powder compacts, placed within the graphite die, are subjected to uniaxial pressure (typically up to 100 MPa) applied through punches. A pulsed DC power supply is connected to the top and bottom punches to facilitate the sintering process[17].

Figure 1.2 shows the SPS setup, while Figure 1.3 schematically illustrates the plasma formation and Joule heating mechanisms involved in the SPS process.

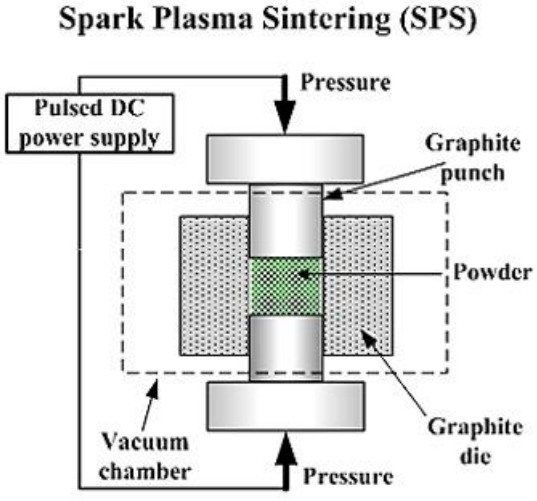

Figure 1.2 Spark Plasma Sintering set up[17].

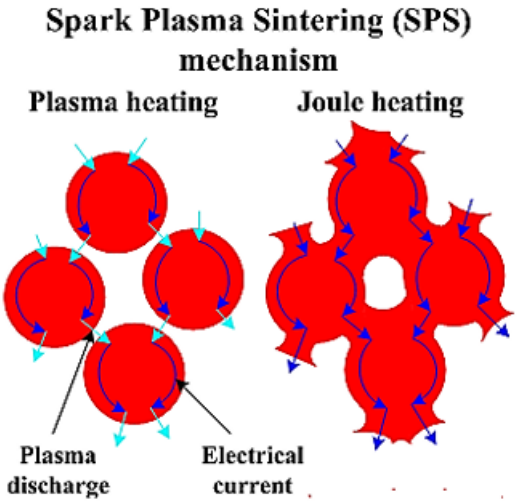

Figure 1.3 Sintering mechanism during SPS[17].

The entire process is usually conducted in an inert atmosphere or vacuum and requires only 5 to 20 minutes, making it a much quicker technique compared to traditional sintering methods.

1.4.2 Key parameter affecting Spark Plasma Sintering

- **Temperature:** In SPS consolidation method, heat is absorbed by the compacted powder, with the energy supplied by the electric current. This process allows for the study of sample density and observation of the influence of sintering temperature on the sintered material. The correlation between density (ρ) and sintering temperature (T) can be described by the following equation[18]:

$$\rho = s\left(\frac{T}{T_m}\right) + b \qquad (1)$$

  Here, 's' represents the slope of the curve, also referred to as temperature sensitivity, T_m denotes the melting point of the material, and 'b' is the intercept of the density axis.

- **Pressure:** In Spark Plasma Sintering (SPS), the uniaxial load plays a significant role in the densification of the final products by offering two distinct advantages. Firstly, pressure facilitates the reshuffling of activated powder particles, which effectively prevents them from agglomerating. Secondly, the applied pressure provides a crucial driving force that enhances the overall sintering process. The impact of pressure on densification can be interpreted using the following equation[4]:

$$\frac{d\rho}{(1-\rho)dt} = B\left(g\frac{\gamma}{x} + P\right) \qquad (2)$$

Here, 't' represents the sintering time, 'B' is an expression that incorporates temperature and the diffusion coefficient, 'γ' denotes the surface energy, 'g' is the geometrical constant, 'x' is a parameter representing particle size, and 'P' signifies the external applied pressure.

- **Heating rate:** High rate of heating during sintering decreases both the grain size and the manufacturing time. Furthermore, a high heating rate enhances the sinterability of the material, initiating the activation of powder particles, which leads to neck formation through grain surface diffusion[19].

1.4.3 Comparison with SPS and Conventional techniques

Table 1 Comparison with SPS and conventional techniques

Parameter	Conventional Sintering	Spark Plasma Sintering (SPS)
Heating Mechanism	External heating via furnace	Internal Joule heating via pulsed DC current
Heating Rate	Slow (5–20 °C/min)	Rapid (up to 1000 °C/min)
Sintering Temperature	High (due to slow diffusion)	Lower (enhanced diffusion from current and pressure)
Sintering Time	Several hours	Few minutes
Pressure Application	Optional or limited	Applied uniaxial pressure (typically 20–100 MPa)
Grain Growth	Significant due to prolonged high temperature	Minimal due to rapid processing
Microstructure Control	Limited	Excellent
Energy Efficiency	Low	High
Applicability	Traditional ceramics and metals	Nanostructured, amorphous, and reactive materials
Atmosphere Control	Required (often inert gases)	Vacuum or inert atmosphere

1.5 Significance of Fe-Based Systems

Fe-based systems are important due to their excellent combination of mechanical strength, magnetic properties, corrosion resistance, and cost-effectiveness. Unlike noble metal-based alloys, Fe-based alloys offer a more economical alternative while still delivering superior performance in demanding environments. Particularly in the form of amorphous or nanocrystalline structures, Fe-based alloys exhibit enhanced soft magnetic behavior, high wear resistance, and thermal stability, making them ideal for applications in transformers, magnetic sensors, biomedical implants, and structural components. Furthermore, their compatibility with advanced processing methods like me MA and SPS enables the development of customized microstructures and tailored properties, expanding their potential for high-performance and functional applications[3], [20], [21].

Chapter 2

Literature Review

2.1 Crystalline alloys: Overview

Crystalline alloys, commonly referred to as traditional metallic alloys, are characterized by a periodic atomic arrangement, contrasting significantly with the disordered structure of amorphous alloys. Crystalline alloys have formed the backbone of metallic materials for structural and functional applications due to their tunable microstructures, well-established processing techniques, and broad mechanical and thermal property ranges.

Recent literature has emphasized the continued importance of crystalline alloys, especially in comparison with their amorphous counterparts. For example, in contrast to amorphous alloys, which are thermodynamically metastable and often require complex processing conditions such as rapid solidification or mechanical alloying to avoid crystallization, crystalline alloys can be readily synthesized and processed using conventional metallurgy approaches like casting, forging, and rolling[22]. Their well-ordered grain structure enables plastic deformation mechanisms such as dislocation motion, twinning, and grain boundary sliding, providing ductility and toughness, which are sometimes limited in amorphous systems.

The evolution of crystalline alloy design has also incorporated insights from multicomponent systems. High-entropy crystalline alloys, for example, adopt face centered cubic (FCC) or body centered cubic (BCC) crystal structures and are stabilized by configurational entropy. These alloys have demonstrated unique combinations of strength, ductility, and corrosion resistance[23]. In some cases, crystalline high-entropy alloys (HEAs) coexist with amorphous phases, offering a hybrid microstructure with improved thermal stability and mechanical response[24].

Despite the growing interest in amorphous alloys due to their superior strength and soft magnetic properties, crystalline alloys maintain significant advantages in terms of scalability, machinability, and thermal stability. Crystalline Fe-based alloys, for instance, remain dominant in power applications due to their high

saturation magnetization, even though amorphous alternatives offer lower core loss at high frequencies[25].

2.2 Fe-based Amorphous Alloys

2.2.1 Composition and Glass-forming Ability (GFA)

Fe-based amorphous alloys are primarily composed of iron as the matrix element with the addition of metalloids such as B, Si, and P, along with minor elements like Cu and Nb to improve glass-forming ability. The high GFA of these alloys is attributed to the presence of multiple alloying elements, significant atomic size mismatch, and negative mixing enthalpies, which hinder crystallization. In particular, systems such as $Fe_{77.7}Si_8B_{10}P_4Cu_{0.3}$ demonstrate superior GFA and thermal stability when processed through methods like gas atomization followed by spark plasma sintering (SPS), with optimized amorphous structure retention below 712 K [25]. Furthermore, mechanical alloying has enabled the production of Fe-based amorphous alloys by bypassing the liquid phase, allowing for amorphization in systems with both negative and slightly positive mixing enthalpies [22].

2.2.2 Mechanical and Thermal Properties

Fe-based amorphous alloys are known for their exceptional hardness, high tensile strength (up to 3.6 GPa), and good wear resistance. Their disordered atomic arrangement restricts dislocation movement, leading to high strength but typically limited ductility. Additionally, they offer high soft magnetic properties, including high permeability and saturation magnetization (e.g., Bs ≈ 1.34 T), making them suitable for magnetic applications in high-frequency environments [25]. Thermal analysis revealed crystallization onset temperatures around 790–830 K, depending on composition, with structural relaxation and nanocrystal formation influencing mechanical and magnetic performance [21]. Controlled nano-crystallization in Fe-based systems can also enhance magnetic properties without significantly compromising the amorphous matrix[26].

Table 2 Review of some Amorphous alloys studied

Alloy System	Bs (T)	Thermal Stability	Magnetostriction	GFA
Fe-based [25], [21]	1.3–1.7	Moderate to High	Moderate	High
Co-based [27]	0.45–0.57	Very High	Near-zero	Moderate
Ni-based [23]	0.5–0.8	Moderate	Low	Moderate
Zr-based [24]	~0.3–0.6	High (Tx ≈ 800–850 K)	Low	Very High
Pd-based [24]	~0.2–0.5	Very High	Low	Excellent
High Entropy (HEAA) [22], [23]	Variable	High (depending on elements)	Variable	Very High
Ti-based [24]	~0.3–0.5	Moderate	Low	High
Mg-based [22]	<0.3	Low	High	Poor

2.3 Mechanical Alloying as a Synthesis Method for Amorphous Alloys

2.3.1 Mechanism of Amorphization

MA is a powerful solid-state synthesis route to produce amorphous alloys by repeated cold welding, fracturing, and rewelding of powder particles in a high-energy ball mill. Unlike rapid solidification techniques that rely on liquid-phase processing, MA can achieve amorphization directly in the solid state, expanding the compositional range and avoiding issues like gravity segregation[22]. The transformation mechanisms can follow either direct amorphization—via solid-state amorphization reactions (SSAR)or indirect paths involving intermediate phases such as intermetallic compounds, solid solutions, nanocrystals.

For example, $Zr_{2.5}FeNiSi_{0.4}B_{0.6}$ alloys synthesized by MA showed transformation from crystalline Ni-type FCC structures to a fully amorphous

phase after prolonged milling [23]. Similarly, the Cu–W and Cu–Ag systems, which have positive mixing enthalpies, were successfully amorphized via MA, something not feasible by melt spinning[22]. These results demonstrate that MA enables amorphization even in thermodynamically unfavorable systems by promoting high defect densities and kinetic barriers to crystallization.

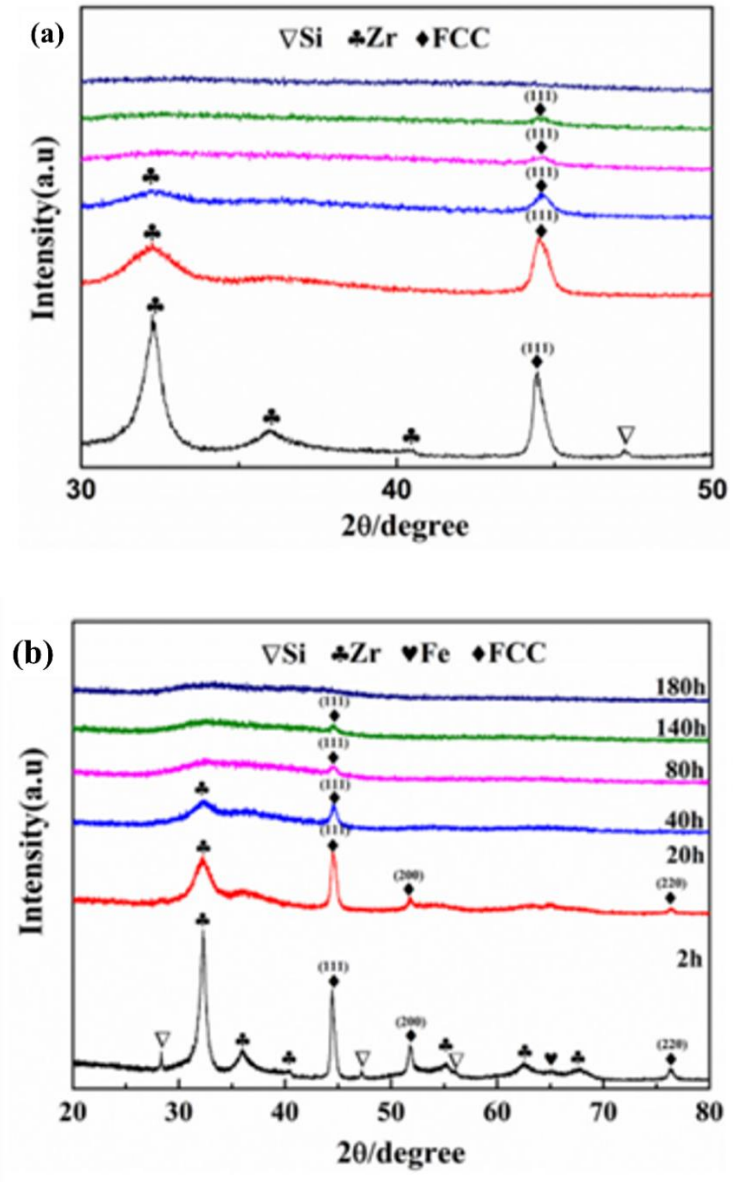

Figure 2.1 XRD patterns of the milled $Zr_xFeNiSi_{0.4}B_{0.6}$ HEAs powders as function of milling times (a) and (b) x=2.5 [23]

2.3.2 Influencing Parameters

The amorphization outcome in MA strongly depends on processing variables. Milling time is critical: in the case of Fe-based amorphous powders (e.g.,

$Fe_{77.7}Si_8B_{10}P_4Cu_{0.3}$), amorphous structure formation was confirmed after extended milling, with DSC curves showing overlapping exothermic peaks at ~795–823 K indicating homogeneous amorphous phases [25]. In $Al_{86}Ni_8Y_6$ systems, amorphization proceeded over 80–200 hours, with over-milling leading to recrystallization due to stored energy release [22].

Milling speed influences collision energy. In $Co_{75}Ti_{25}$, increasing speeds to 3.3 s^{-1} led to undesirable recrystallization, while 2.1 s^{-1} resulted in a fully amorphous phase after 48h of milling [22].

Ball-to-powder ratios (BPR) also affect energy transfer. In Si–B–C–N systems, BPRs from 10:1 to 100:1 enhanced amorphization but introduced contamination from the milling media (e.g., ZrO_2) [22].

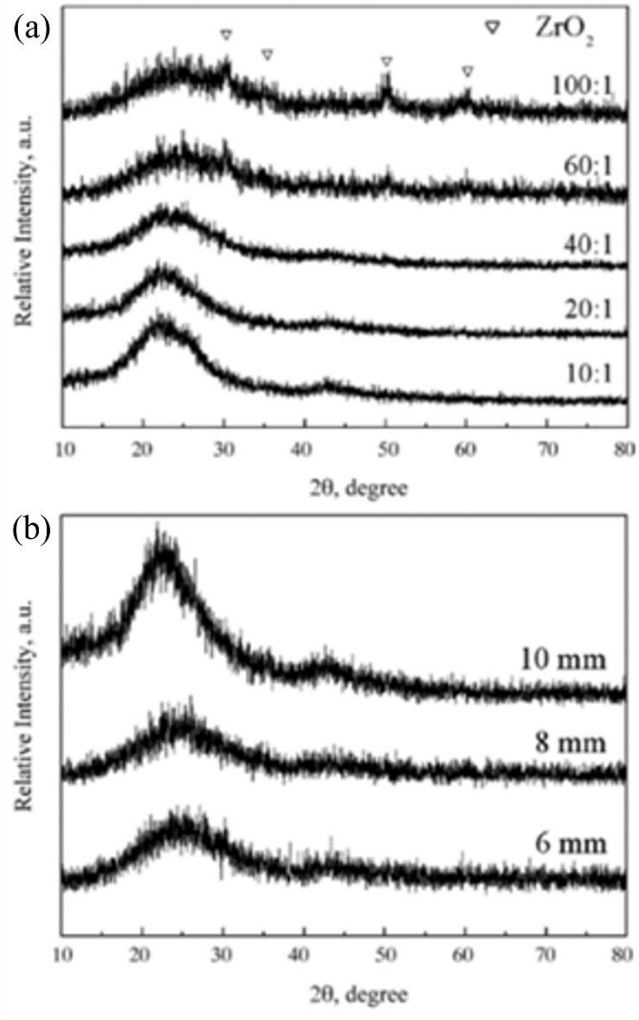

Figure 2.2 XRD patterns for Si-B-C-N samples milled for 10h (a) varying ball-to-powder mass rations, (b) different diameters of milling media. [20]

Cryomilling, a combination of mechanical alloying and low-temperature processing, helped achieve finer grains and reduced thermal crystallization. For example, $Al_{12.6}Si–TiB_2$ composites cryomilled for 30 minutes post-MA showed a ~50% reduction in particle size and improved density (95–96% vs. 90%) [22].

High entropy mixing (e.g., ZrTiCuNiBe) promotes GFA and mechanical stability in Zr-based HEA systems. The alloy $Zr_{2.5}FeNiSi_{0.4}B_{0.6}$ exhibited excellent amorphous phase stability with crystallization temperatures ~689 °C after 180 h of milling [23].

2.4 Spark Plasma Sintering for Consolidation of Amorphous Alloys

2.4.1. Effect of SPS Parameters

SPS is a new powder consolidation method that utilizes high pulsed DC and uniaxial pressure to achieve rapid densification at lower temperatures and reduced holding times compared to conventional sintering. Critical SPS parameters sintering temperature (Ts), heating rate, holding time, pressure, and atmosphere directly impact densification, structural evolution, and magnetic properties of amorphous alloys.

For instance, $Fe_{77.7}Si_8B_{10}P_4Cu_{0.3}$ amorphous powders consolidated at Ts = 696–712 K, with a heating rate of 100 K/min and pressure of 800 MPa, achieved relative densities up to 94%, without significant crystallization [25]. Compared to conventional methods, SPS reduces porosity effectively due to its high heating rates and pressure-induced plastic flow. A similar approach was seen in previous studies on Fe-based amorphous ribbons using warm compaction or hot pressing, which showed inferior magnetic properties due to structural relaxation and partial crystallization [21].

2.4.2 SPS of Amorphous Alloys

SPS is particularly well-suited for the consolidation of Fe-based amorphous alloys, offering fast densification while preserving soft magnetic performance. In the SPS-processed $Fe_{77.7}Si_8B_{10}P_4Cu_{0.3}$ compact, soft magnetic properties were retained with saturation magnetic flux density (Bs) of 1.34 T and permeability (μ) of 163 at 20 kHz, making it viable for high-frequency applications [25].

Key to this success is the use of gas atomized spherical powders with good glass-forming ability (GFA), which enhances compaction uniformity and isotropy compared to flake powders often used in other compaction approaches [21], [26]. In contrast, flake-based amorphous compacts consolidated by hot pressing often showed anisotropy in magnetic response and higher losses due to microcrack formation and texture alignment [26].

2.4.3 Challenges in Preserving Amorphous Structure during SPS

One of the major challenges in SPS consolidation of amorphous materials is preventing crystallization during sintering. Even when the bulk sintering temperature is kept below the crystallization onset temperature (Tx), localized overheating due to Joule heating and poor thermal conductivity of powders may cause partial or full crystallization.

For example, in $Fe_{77.7}Si_8B_{10}P_4Cu_{0.3}$, samples sintered above 725 K exhibited diminished DSC exothermic peaks and clear crystalline diffraction peaks in XRD patterns, indicating structural degradation [25]. Similarly, prior work on consolidated Zr- and Fe-based bulk metallic glasses (BMGs) also showed that holding times greater than a few minutes at elevated temperatures caused structural relaxation and crystalline phase formation, leading to deteriorated magnetic and mechanical performance [24], [21].

Additional issues, such as non-uniform current distribution, temperature gradients between die and sample, and interfacial reactions, can further complicate amorphous retention. Use of short holding times (near-zero), rapid heating and cooling, and pre-optimization of powder composition (e.g., higher B and P content to boost GFA) have been shown to mitigate these effects [25], [23].

2.5 Objective

The main aim of this study is to prepare and characterize Fe-based amorphous powders prepared via mechanical alloying and then consolidated by SPS. The objectives of the research are as follows:

- To investigate the amorphization behavior of a Fe-based ternary system via mechanical alloying.

- To study the phase formation during the MA process.
- To examine the phase evolution during the sintering of amorphous powder using SPS.
- To evaluate the mechanical properties of the sintered samples through Vickers hardness.

Chapter 3

Methodology

The methodology for this study involves a sequence of stages starting from the selection of elemental powders, followed by MA, powder characterization, SPS, and final material characterization. A schematic flowchart outlining the complete experimental process is provided below:

Flowchart

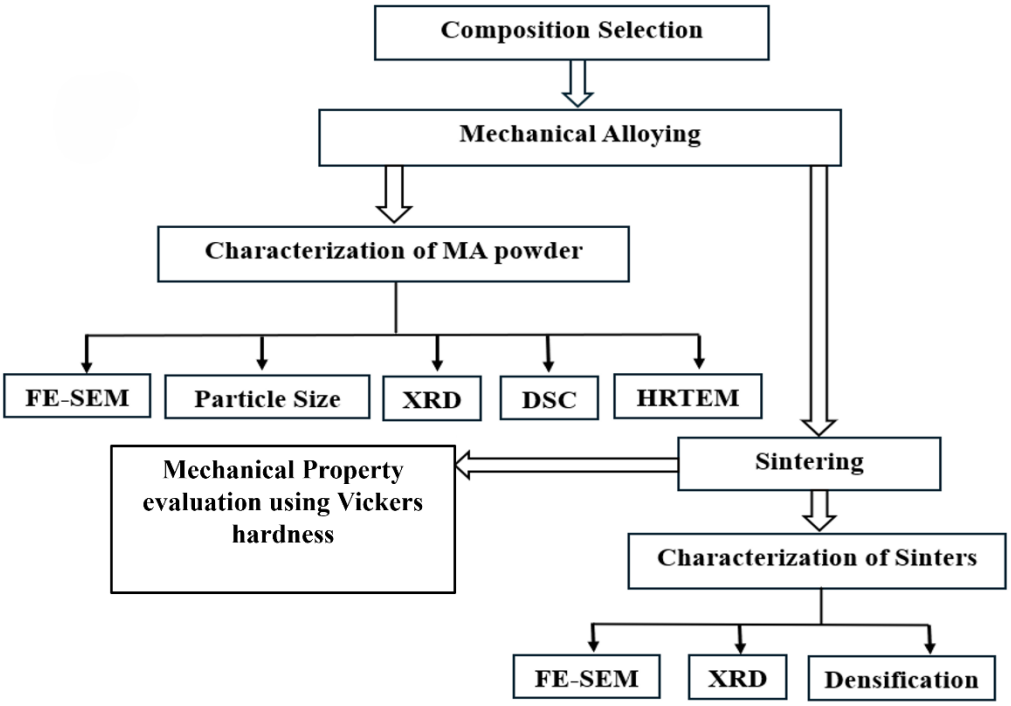

3.1 Composition Selection

The ternary phase diagram (Figure 3.1) of the Fe–Al–Ti system was used to identify a Fe-rich single-phase BCC_B2 region. From this stable phase region, two compositions $Fe_{72}Al_{26}Ti_2$ (at. %) and $Fe_{54}Al_{43}Ti_3$ (at. %) were selected to study the phase formation, microstructure, and densification during MA and SPS.

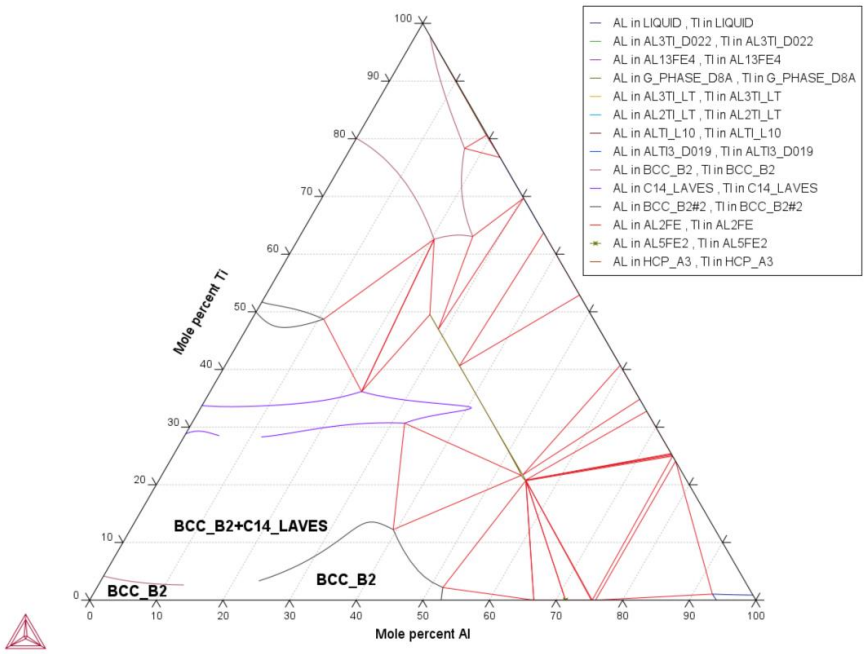

Figure 3.1 Fe-Al-Ti isothermal ternary phase diagram

Elemental powders of Fe (99.5%, 200 mesh, Sisco Research Laboratories), Al (99.5%, 325 mesh, SRL), and Ti (99.9%, 150 mesh, Alfa Aesar) were used. The powders were weighed and mixed in their respective compositions using an electronic balance.

Table 3 Elemental compositions of Fe-Al-Ti samples

Elements	Sample 1		Sample 2	
	at. %	wt. %	at. %	wt. %
Fe	72	83.453	54	69.815
Al	26	14.560	43	26.860
Ti	2	1.987	3	3.325

3.2 Mechanical Alloying

3.2.1 Process

Mechanical alloying was conducted in a planetary ball mill (PM 200, Retsch GmbH, Germany) (Figure 3.2) using hardened steel vials and 10 mm hardened steel balls. The process was carried out at a disc speed of 300 RPM and a ball-to-powder ratio (BPR) of 10:1. To prevent cold welding and enhance milling efficiency, toluene (75 ml) and stearic acid (0.08 wt.%) were used as process

control agents. Milling was performed for up to 80 hours, with intermediate samples collected at 1 h, 20 h, 40 h, 60 h and 80 h for microstructural analysis.

Table 4 Variable of ball milling process

Parameter	Details
Vial Material	Hardened Steel
Ball Material	Hardened Steel
Ball Diameter	10 mm
BPR	10:1
Disc Speed	300 RPM
Milling Duration	Up to 80 hours
PCAs	Toluene (75 ml), Stearic Acid (0.08 wt.%)
Sampling Intervals	1h, 20h, 40h, 60h, 80h

Figure 3.2 Planetary ball mill (PM 200, Retsch GmbH, Germany)

3.2.2 MA powder characterization

a) X-Ray diffraction studies

Phase identification of the ball-milled powder and sintered samples was carried out using a Panalytical Empyrean Alpha 1 diffractometer equipped with Cu-Kα radiation (λ = 0.154 nm). The XRD scans were recorded over an appropriate 2θ range from 20 º to 80 º at a fixed step size and scan rate. The obtained diffraction patterns were analyzed to identify the crystalline phases and assess the degree of amorphization**.**

b) Morphology

The morphologies of both the sintered and powder samples were examined using a field emission scanning electron microscope (JEOL IT800). The chemical composition of the samples was analyzed using an energy dispersive spectrometer (EDS) integrated with the FE-SEM system.

c) Particle size analysis

Particle size analysis was performed using ImageJ software based on the circular method, where particles were manually outlined and analyzed to determine their equivalent circular diameters.

d) Differential Scanning Calorimetry (DSC)

The phase transformations and thermal stability of the powders were investigated using DSC (PerkinElmer STA 8000). The measurements were conducted in a nitrogen (N_2) atmosphere, with specimens heated at a rate of 10 °C/min up to 1000 °C.

e) Transmission Electron Microscopy (TEM)

TEM (JEOL JEM-2100) was used to examine the amorphous and crystalline nature of the mechanically alloyed powder particles. High-resolution image and selected area electron diffraction (SAED) were employed to distinguish between amorphous and crystalline phases.

f) Densification

The density of the sintered samples was measured using Archimedes' principle, with distilled water serving as the immersion medium. The bulk density values obtained were then compared with the theoretical

densities to assess how effectively the samples were densified during the sintering process.

3.3 Consolidation of Ball-Milled Powders via SPS

The ball-milled powders were consolidated using SPS (FCT Systeme GmbH, Germany) in a graphite die with an inner diameter of 20.4 mm and punch of 20 mm diameter. Consolidation was carried out at four different temperatures 300°C, 800°C, 1000°C, and 1200°C for the $Fe_{83.453}Al_{14.560}Ti_{1.987}$ composition, and at 350°C, 800°C, 1000°C and 1200°C for $Fe_{69.815}Al_{26.860}Ti_{3.325}$ composition. Each consolidation was performed with a holding time of 5 min and a heating rate of 100 °C/min. Sintering was performed under vacuum conditions with a constant uniaxial pressure of 38 MPa. To ensure easy removal of the compacted samples and to minimize temperature inhomogeneities, 0.2 mm thick graphite foils were placed between the punches and powders, as well as between the die and powders.

Figure 3.3 Spark Plasma Sintering (FCT Systeme GmbH, Germany)

3.4 Mechanical Properties

3.4.1 Microhardness

Hardness tester (MMV-A) was used to determine the Vickers microhardness of the polished samples. A load of 2000 gf was applied with a dwell time of 20 seconds for each hardness measurement. The average microhardness value for each sintered sample was calculated from five individual readings, along with the corresponding standard deviation to represent the variability in measurements.

Chapter 4

Results and Discussion

4.1 Phase evaluation during mechanical alloying

Figure 4.1(a) and Figure 4.1(b) display the X-ray diffraction (XRD) patterns of $Fe_{83.453}Al_{14.560}Ti_{1.987}$ and $Fe_{69.815}Al_{26.860}Ti_{3.325}$ powders, respectively, milled for different durations (1 h, 20 h, 40 h, 60 h, and 80 h). For both compositions, the XRD pattern at 1 hour reveals sharp and intense peaks corresponding to the elemental phases of Fe, Al, and Ti, indicating the crystalline nature of the unalloyed starting powders. As the milling time progresses, the intensity of these peaks gradually diminishes and becomes increasingly broadened, accompanied by the disappearance of Ti peaks. This trend is indicative of extensive alloying and nanocrystalline refinement due to repeated cold welding and fracturing typical of the mechanical alloying process. At extended milling times (60 h and 80 h), the diffraction patterns display broad, low-intensity humps, characteristic of the formation of an amorphous phase.

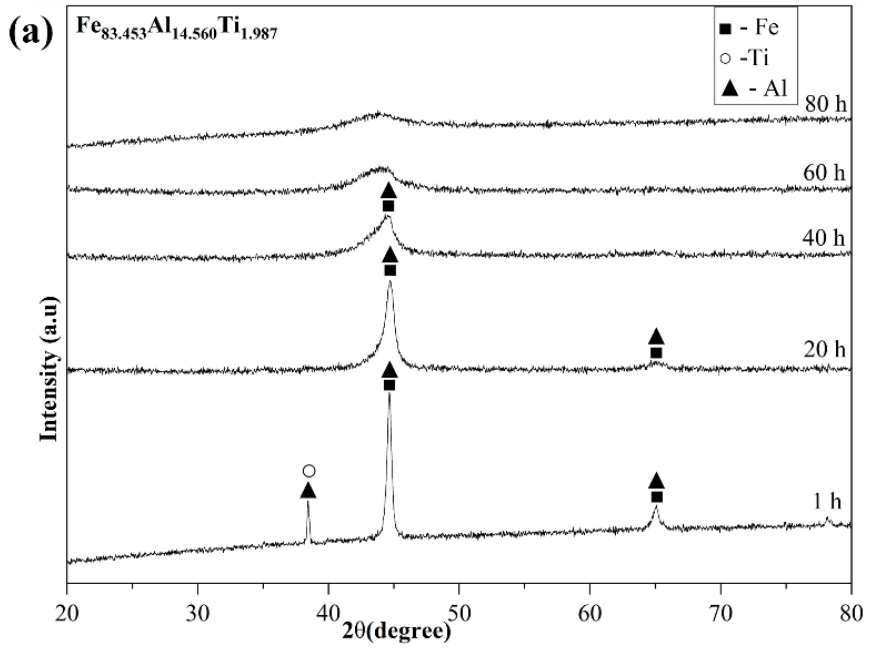

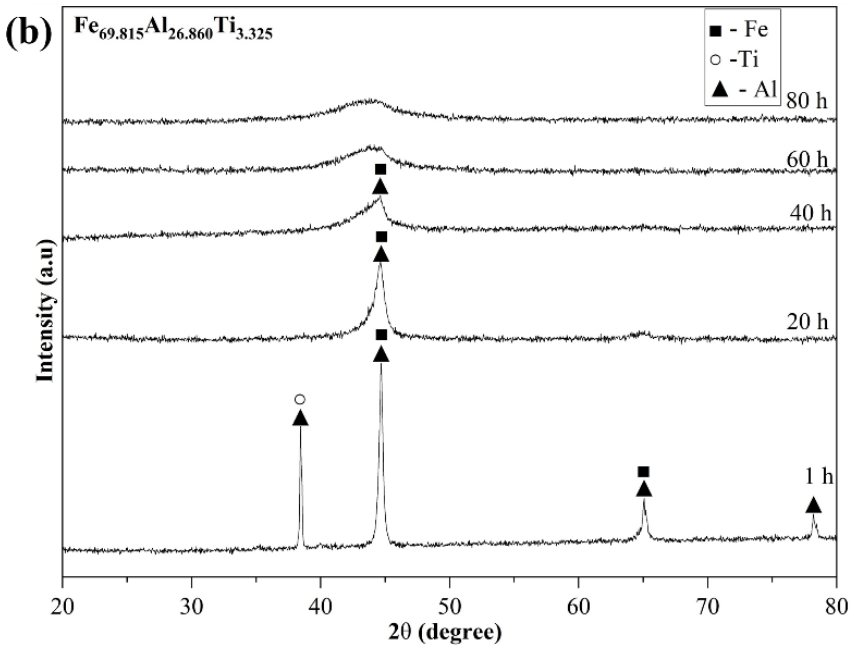

Figure 4.1 XRD patterns of (a) $Fe_{83.453}Al_{14.560}Ti_{1.987}$ and (b) $Fe_{69.815}Al_{26.860}Ti_{3.325}$ powders revealing phase evolution during mechanical alloying up to 80 h

The transition from crystalline to amorphous structure is more evident in the $Fe_{83.453}Al_{14.560}Ti_{1.987}$ composition, suggesting a relatively higher glass-forming ability compared to the $Fe_{69.815}Al_{26.860}Ti_{3.325}$ composition. This could be attributed to differences in elemental ratios, particularly the lower Al content and more favorable atomic size mismatch, which can enhance amorphous phase stability.

4.2 High-Resolution TEM image and corresponding SAED pattern confirming partial amorphous nature

Figure 4.2 shows the SAED and HRTEM images of the $Fe_{83.453}Al_{14.560}Ti_{1.987}$ powder after 80 hours of MA. The SAED pattern of Figure 4.2 (a) exhibits a diffuse halo which is normally characteristics of an amorphous structure, but the existence of a few diffraction spots clearly signifies the survival of nanocrystalline zones. Also Figure 4.2 (b) presents a barely more spread-out ring without any apparent spots, hence proving that it is partially amorphous.

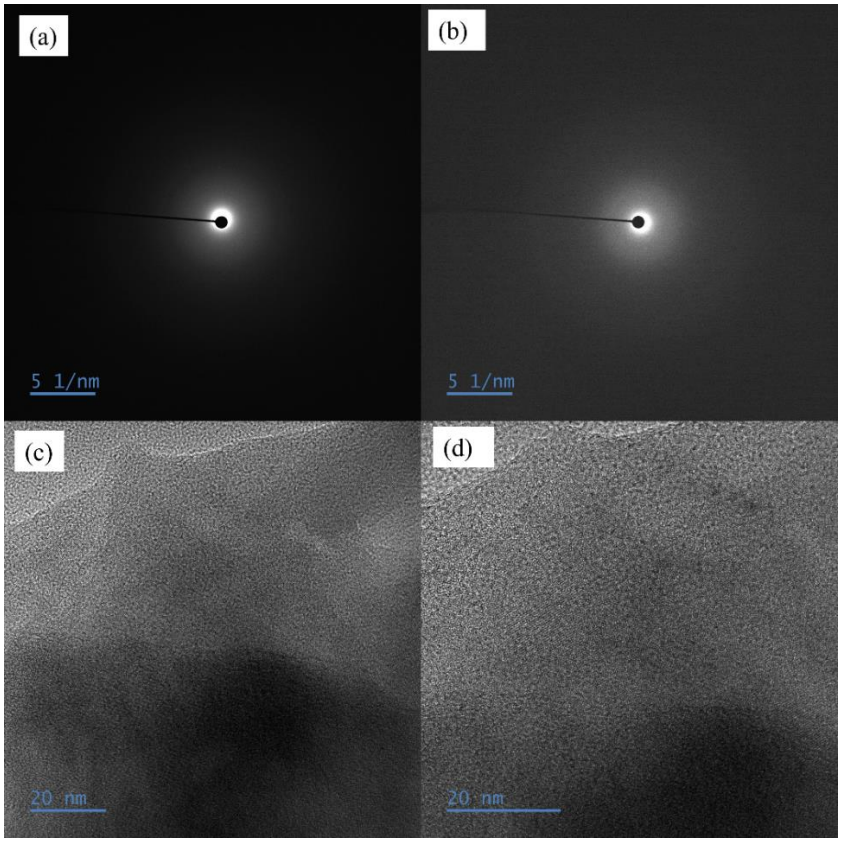

Figure 4.2 Results of SAED (a, b) patterns and HRTEM images (c, d) of 80 h mechanically alloyed $Fe_{83.453}Al_{14.560}Ti_{1.987}$ powder

The HRTEM micrographs in Figure 4.2(c, d) also support the partially amorphous character of the sample. The image mainly consists of some fringes which clear the presence of some crystalline character. These observations all support the fact that the sample is partially amorphous.

4.3 SEM–EDS Characterization of Milled Fe-Based Powders

The morphological evolution and elemental distribution of the $Fe_{83.453}Al_{14.560}Ti_{1.987}$ powder during mechanical alloying were investigated through SEM and EDS analyses, as shown in Figures 4.3.1 (a–e) and (a2–e2). At 1 hour of milling [Figures 4.3.1 (a, a2)], the powders exhibited large, irregular particles resembling the original elemental morphology. These particles showed signs of initial deformation with relatively smooth surfaces and minimal mixing, as confirmed by EDS, which revealed distinct Fe-, Al-, and Ti-rich regions. Upon milling for 20 hours [Figures 4.3.1 (b, b2)], a noticeable refinement in particle size was observed due to increased fracturing. The particles became more irregular and agglomerated due to cold welding, though elemental segregation remained evident, indicating incomplete alloying.

After 40 hours [Figures 4.3.1 (c, c2)], the powders displayed significantly finer and more equiaxed morphology. The particles had undergone sufficient fracturing and welding cycles, resulting in lamellar structures and partial homogenization. EDS mapping at this stage showed improved elemental intermixing. Continued milling to 60 hours [Figures 4.3.1 (d, d2)] led to a highly refined microstructure with near-spherical and dense particles, and the average size approached a steady-state value. EDS results revealed a near-uniform distribution of Fe, Al, and Ti within individual particles, highlighting the advanced stage of alloying.

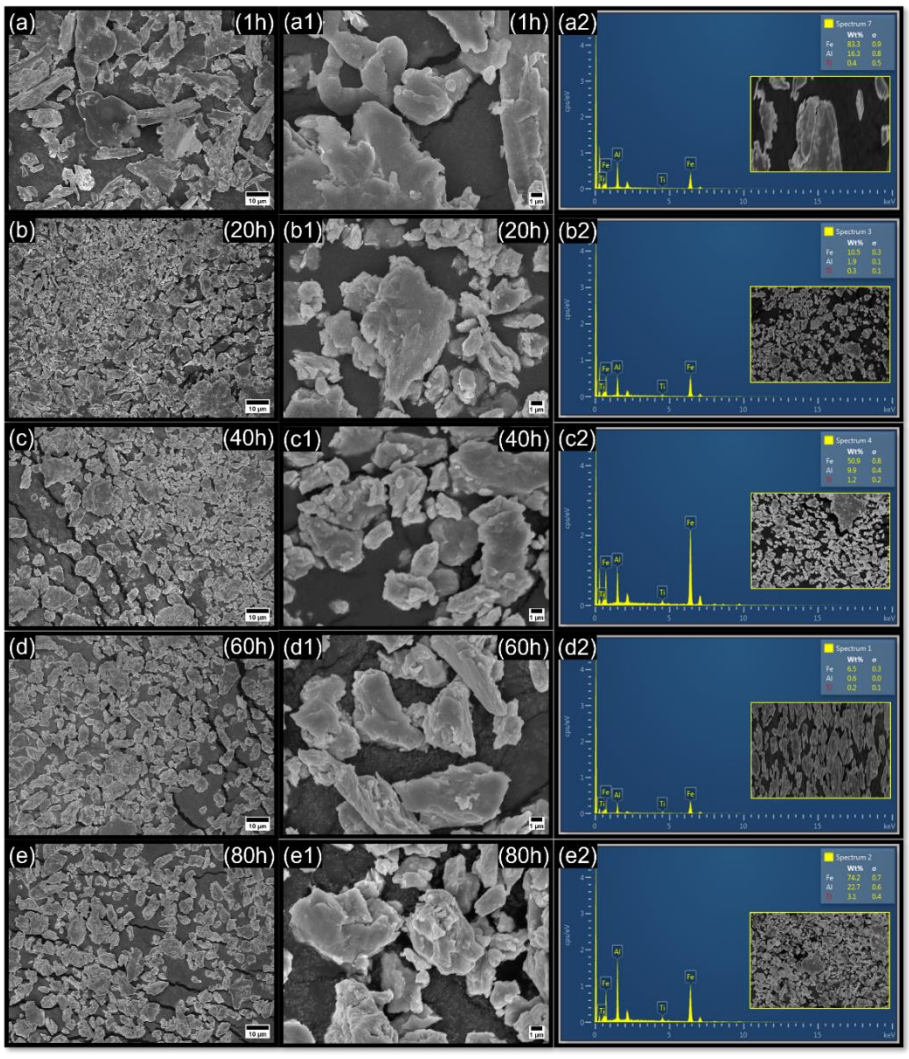

Figure 4.3.1 SEM image and EDS result of $Fe_{83.453}Al_{14.560}Ti_{1.987}$ at 1h, 20h, 40h, 60h and 80h milled powder.

After 80 hours of milling [Figures 4.3.1 (e, e2)], the particles appeared further refined with some agglomeration, a result of excessive cold welding. The

powders showed dense, uniform morphology, indicating extensive mechanical alloying. EDS confirmed excellent compositional homogeneity, marking the formation of a nearly fully alloyed powder. These observations collectively demonstrate the progressive refinement and alloying achieved during prolonged mechanical milling.

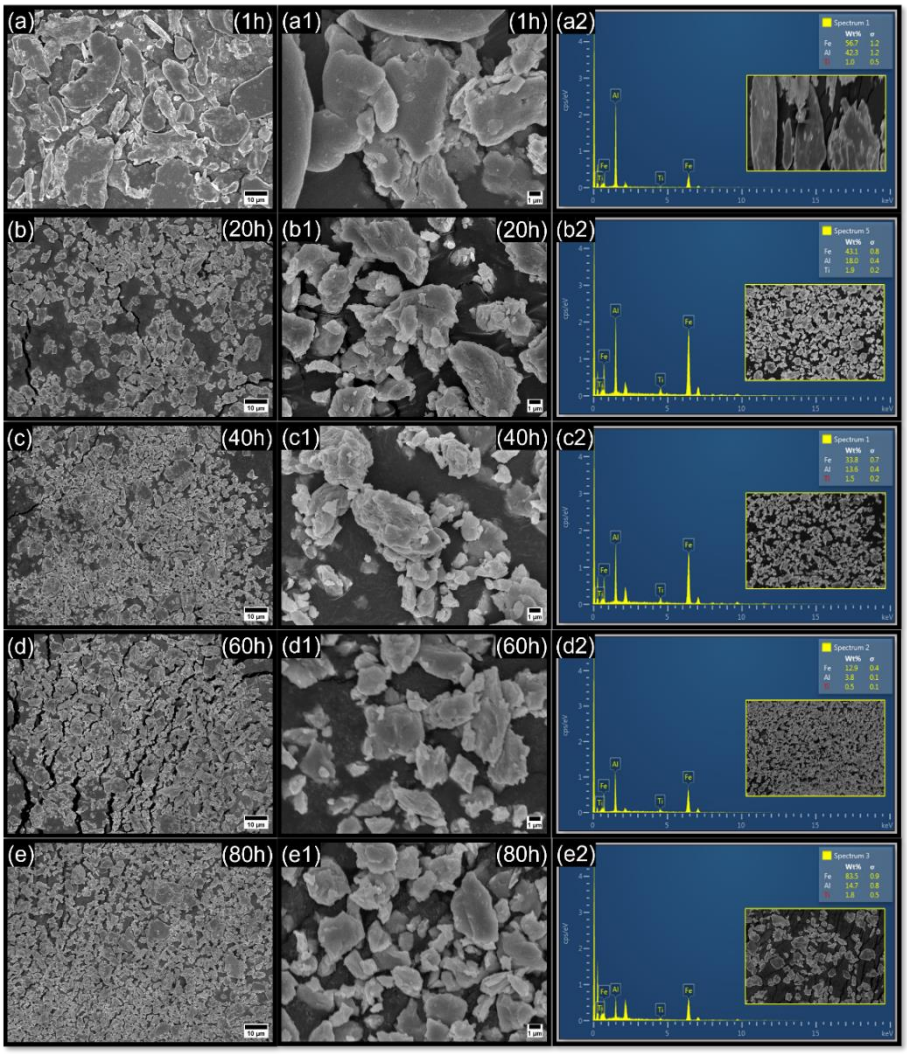

Figure 4.3.2 SEM image and EDS result of $Fe_{69.815}Al_{26.860}Ti_{3.325}$ at 1h, 20h, 40h, 60h and 80h milled powder.

The progressive structural transformation of $Fe_{69.815}Al_{26.860}Ti_{3.325}$ powders during mechanical alloying is evident from the SEM and EDS analyses. At the initial stage of 1-hour milling [Figure 4.3.2 (a, a2)], the powders largely retained their original elemental morphology, exhibiting large, irregular particles with smooth surfaces, and EDS results indicated poor elemental mixing with distinct Fe, Al, and Ti-rich zones. After 20 hours of milling [Figure 4.3.2(b, b2)], more

intense plastic deformation and fracturing were observed, accompanied by the onset of cold welding, resulting in smaller, more irregular particles forming layered composite structures. Elemental intermixing had begun but remained incomplete. By 40 hours [Figure 4.3.2 (c, c2)], the particles became finer, more equiaxed, and displayed significant refinement, with layered internal structures due to repeated fracturing and welding. EDS analysis at this stage showed a more uniform distribution of Fe, Al, and Ti within individual particles. At 60 hours [Figure 4.3.2 (d, d2)], the powders reached a near steady-state particle size, displaying compact, possibly spherical morphologies, suggesting advanced homogenization and potential amorphous phase formation. Finally, after 80 hours of milling [Figure 4.3.2 (e, e2)], the powders appeared highly refined and densely packed, although a slight increase in average particle size was observed, likely due to cold welding and agglomeration—an effect more pronounced in this high-Al composition. EDS results confirmed excellent compositional homogeneity, indicating the successful formation of a fully alloyed powder suitable for further consolidation processes like spark plasma sintering.

4.4 Particle Size Variation During Mechanical Alloying

Figure 4.4 shows average particle sizes diameter was found to be 8.16 ± 4.39 µm, 3.32 ± 1.33 µm, 3.27 ± 1.20 µm, 4.45± 1.42 µm and 5.17 ± 1.81 µm, respectively for 1h, 20h, 40h, 60h and 80h mechanically alloyed $Fe_{83.453}Al_{14.560}Ti_{1.987}$ powder particles. In case of 1h, 20h, 40h, 60h and 80h mechanically alloyed $Fe_{69.815}Al_{26.860}Ti_{3.325}$ powder particles, the average particle sizes were 11.17 ± 5.12 µm, 4.63 ± 1.47 µm, 3.77 ± 1.12 µm, 3.06 ± 1.03 µm and 3.57 ± 41.06 µm respectively. The plot in Figure 5 represents the variation of average particle size with progress of

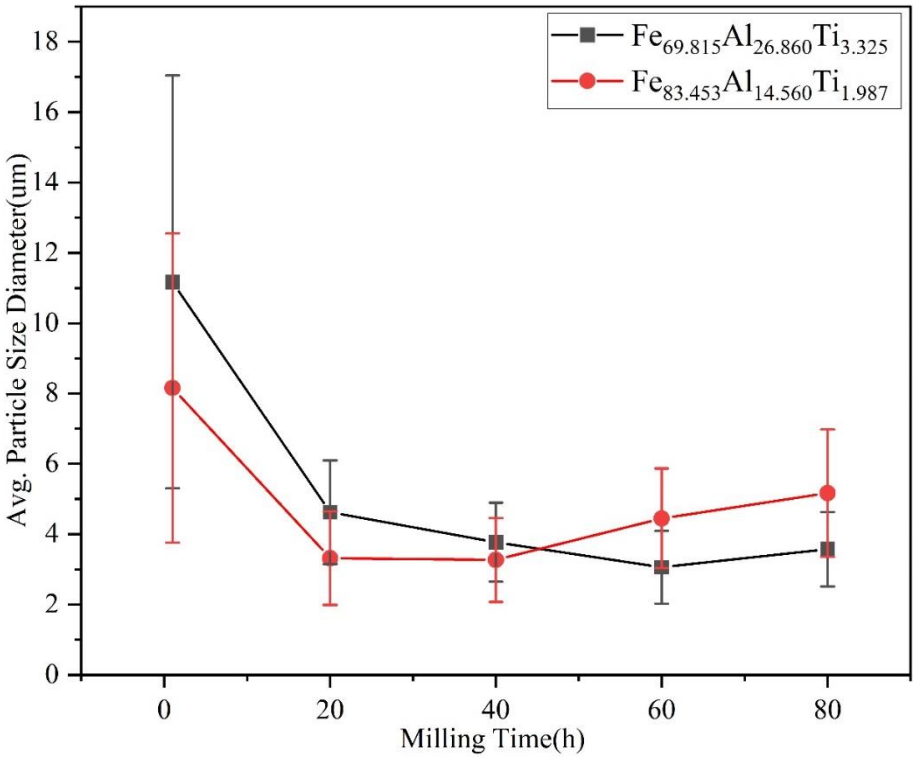

Figure 4.4 Variation of average particle size diameter with time of mechanical alloying for $Fe_{83.453}Al_{14.560}Ti_{1.987}$ and $Fe_{69.815}Al_{26.860}Ti_{3.325}$ powder compositions.

mechanical alloying. It can be observed that for powder $Fe_{83.453}Al_{14.560}Ti_{1.987}$ decrease in particle size for 1-20 h, 20-40 h there is stability in particle and 40-80 h slightly increase in particle size and for powder $Fe_{69.815}Al_{26.860}Ti_{3.325}$ decrease in particle size for 1-60 h and slightly increase in particle size for 60-80 h. The metallic powder particles are of ductile in nature and hence can absorb the impact energy of the grinding balls during ball milling at the initial stage. As the defect density increases with time, the particles get more and more brittle and after a certain duration of milling the defect density reaches a saturation stage which leads to saturation in breaking of particles. Thus, higher rate of decrease in particle size was observed during 1-20 h and increase in particle size because of cold welding and agglomeration.

4.5 Thermal behavior of amorphous powder

Figure 4.5 shows the combined DSC heating curves of both Fe-based alloy powders. The gradual increase in heat flow with temperature confirms that these are heating profiles. For the $Fe_{83.453}Al_{14.560}Ti_{1.987}$ powder, an endothermic peak is observed in the range of 306 °C to 375 °C, indicating a phase transformation occurring within this temperature interval—likely related to the crystallization

of the partially amorphous structure. Similarly, for the $Fe_{69.815}Al_{26.860}Ti_{3.325}$ powder, the endothermic region appears between 340 °C and 415 °C, suggesting that phase transformation in this composition occurs at a slightly higher temperature range.

The change in the transformation range for the $Fe_{69.815}Al_{26.860}Ti_{3.325}$ powder can be explained by its increased content of aluminum, which raises the thermal stability and glass-forming ability of the alloy.

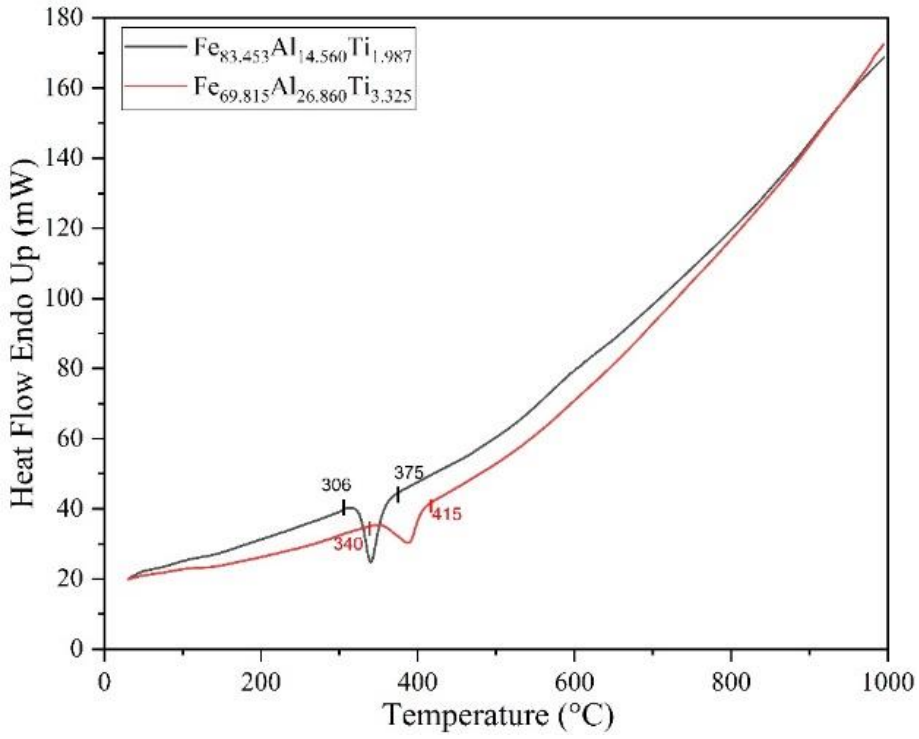

Figure 4.5 DSC curve to identify the phase transformations for $Fe_{83.453}Al_{14.560}Ti_{1.987}$ and $Fe_{69.815}Al_{26.860}Ti_{3.325}$ powder compositions.

4.6 Consolidation of Mechanically Alloyed Powders via SPS

After characterization of powder samples like XRD, SEM, DSC, average particle size and TEM analysis we make sintered sample of both the MA powder using SPS. Figure 4.6 shows a sintered sample of $Fe_{83.453}Al_{14.560}Ti_{1.987}$ [Figure 4.6(a)]and $Fe_{69.815}Al_{26.860}Ti_{3.325}$ [Figure 4.6(b)] powder at different temperatures. Both the mechanically alloyed powders were consolidated via SPS using graphite die and punch of 20 mm diameter. The 80 h mechanically alloyed powders were sintered at 4 different temperatures 300°C, 800°C, 1000°C and 1200°C and the other 80 h mechanically alloyed powders were

sintered at four different temperatures 350°C, 800°C, 1000°C and 1200°C at constant pressure of 38 MPa. The heating rate and holding time at the sintering temperatures were maintained at 100 °C/min and 5 min, respectively.

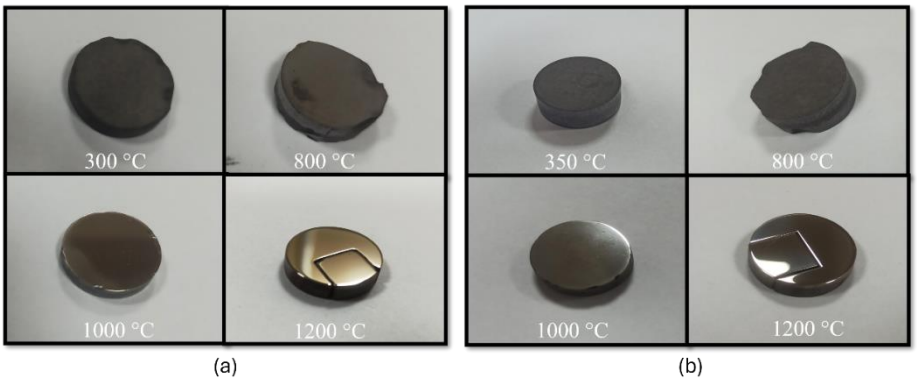

Figure 4.6 Consolidated solid sample at different temperatures of powder (a) $Fe_{83.453}Al_{14.560}Ti_{1.987}$ at 300 °C, 800 °C, 1000 °C, 1200 °C and (b) $Fe_{69.815}Al_{26.860}Ti_{3.325}$ at 350 °C, 800 °C, 1000 °C, 1200 °C.

4.7 Density variation with sintering temperature

Figure 4.7 illustrates the variation in sample density with sintering temperature for two different Fe-based compositions— $Fe_{83.453}Al_{14.560}Ti_{1.987}$ [Figure 4.7(a)] and $Fe_{69.815}Al_{26.860}Ti_{3.325}$ [Figure 4.7(b)]. In both compositions, a consistent trend is observed where the practical density increases with rising sintering temperature, approaching the theoretical density. This improvement in densification is attributed to enhanced atomic mobility and diffusion at elevated temperatures, which promote inter-particle bonding and pore elimination.

For the $Fe_{83.453}Al_{14.560}Ti_{1.987}$ sample, the practical density increased from 3.24 g/cm³ at 300 °C to 5.76 g/cm³ at 1200 °C, corresponding to a porosity reduction from 54% to 18%. Similarly, for the $Fe_{69.815}Al_{26.860}Ti_{3.325}$ composition, the density improved from 3.04 g/cm³ at 350 °C to 4.93 g/cm³ at 1200 °C, reducing porosity from 52% to 22.6%.

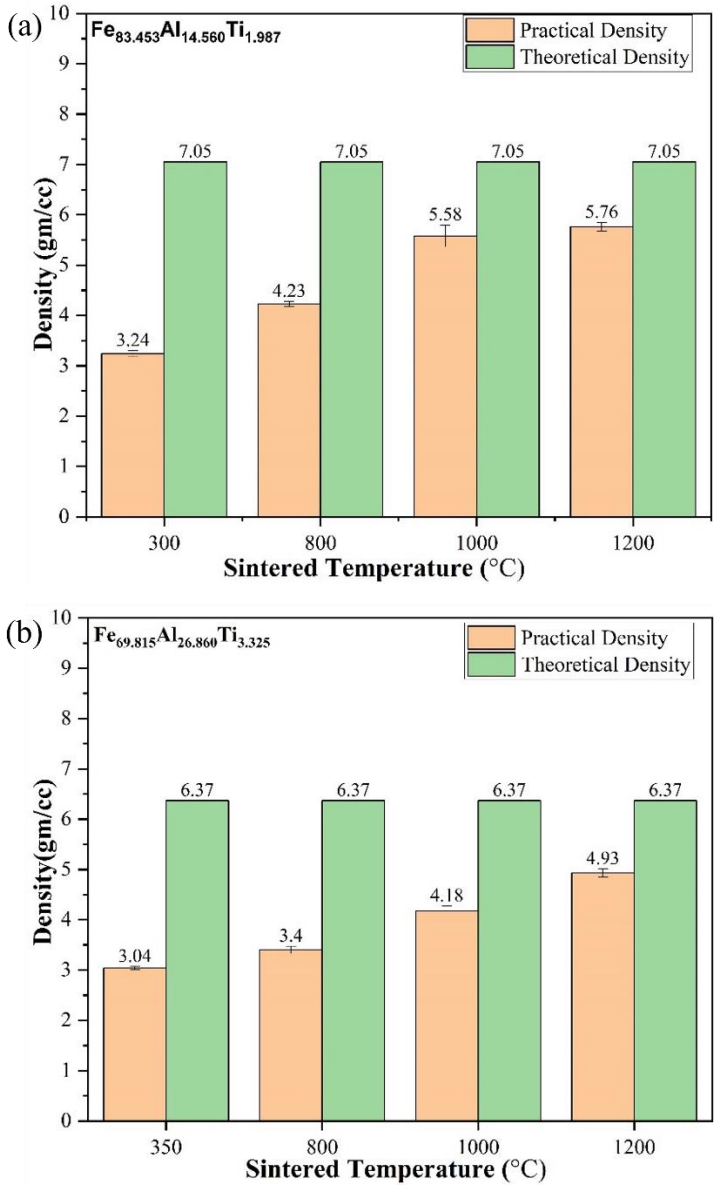

Figure 4.7 Density variation of consolidated samples at different temperatures comparing theoretical and practical densities

Figure 4.7 illustrates the variation in sample density with sintering temperature for two different Fe-based compositions— $Fe_{83.453}Al_{14.560}Ti_{1.987}$ [Figure 4.7(a)] and $Fe_{69.815}Al_{26.860}Ti_{3.325}$ [Figure 4.7(b)]. In both compositions, a consistent trend is observed where the practical density increases with rising sintering temperature, approaching the theoretical density. This improvement in densification is attributed to enhanced atomic mobility and diffusion at elevated temperatures, which promote inter-particle bonding and pore elimination.

For the $Fe_{83.453}Al_{14.560}Ti_{1.987}$ sample, the practical density increased from 3.24 g/cm³ at 300 °C to 5.76 g/cm³ at 1200 °C, corresponding to a porosity reduction from 54% to 18%. Similarly, for the $Fe_{69.815}Al_{26.860}Ti_{3.325}$ composition, the density improved from 3.04 g/cm³ at 350 °C to 4.93 g/cm³ at 1200 °C, reducing porosity from 52% to 22.6%.

Despite these improvements, the practical density for both samples remained lower than the theoretical values (7.05 g/cm³ for $Fe_{83.453}Al_{14.560}Ti_{1.987}$ and 6.37 g/cm³ for $Fe_{69.815}Al_{26.860}Ti_{3.325}$), indicating incomplete consolidation and residual porosity. Notably, the $Fe_{83.453}Al_{14.560}Ti_{1.987}$ samples consistently showed better densification, likely due to their lower Al and Ti content, which reduces oxide formation and enhances diffusion during sintering.

4.8 Phase evolution of sintered Samples with temperature (XRD Analysis)

Figure 4.8 shows the X-ray diffraction (XRD) patterns of sintered $Fe_{83.453}Al_{14.560}Ti_{1.987}$ [Figure 4.8(a)] and $Fe_{69.815}Al_{26.860}Ti_{3.325}$ [Figure 4.8(b)] samples at various sintering temperatures (300 °C/350 °C, 800 °C, 1000 °C, and 1200 °C).

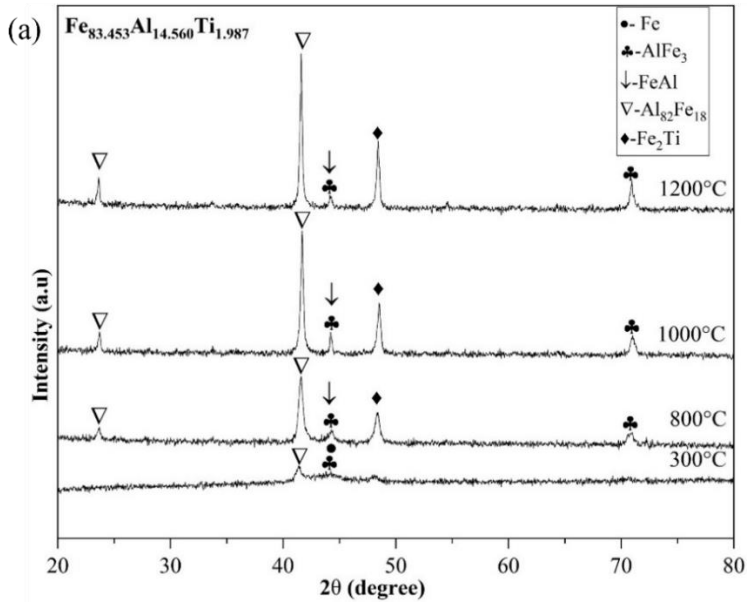

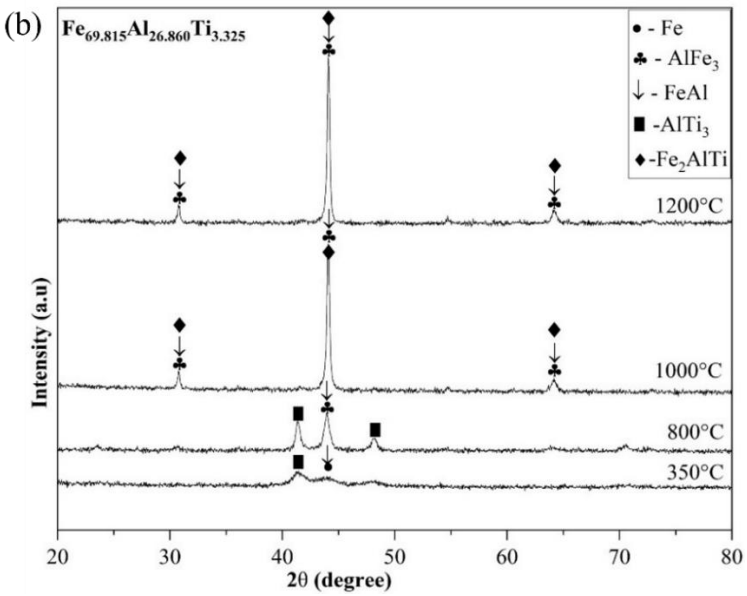

Figure 4.8 Phase evolution of sintered samples at different temperatures analyzed by XRD

Figure 4.8 shows the X-ray diffraction (XRD) patterns of sintered $Fe_{83.453}Al_{14.560}Ti_{1.987}$ [Figure 4.8(a)] and $Fe_{69.815}Al_{26.860}Ti_{3.325}$ [Figure 4.8(b)] samples at various sintering temperatures (300 °C/350 °C, 800 °C, 1000 °C, and 1200 °C). For both compositions, the XRD spectra reveal significant evolution in phase composition as the sintering temperature increases. At lower temperatures (300 °C/350 °C and 800 °C), peaks correspond to initial elemental and simple intermetallic phases such as Fe, $AlFe_3$, and FeAl dominate. However, as the sintering temperature increases to 1000 °C and 1200 °C, new peaks emerge, signifying the formation of more complex intermetallic compounds like Fe_2Ti, $AlTi_3$, and Fe_2AlTi.

The increasing intensity and sharpness of these peaks with temperature suggests improved crystalline and enhanced atomic diffusion during sintering. Specifically, the $Fe_{69.815}Al_{26.860}Ti_{3.325}$ composition [Figure 4.8(b)] exhibits the formation of $AlTi_3$ and Fe_2AlTi at elevated temperatures, while the $Fe_{83.453}Al_{14.560}Ti_{1.987}$ composition [Figure 4.8(a)] shows the presence of $Al_{82}Fe_{18}$ and Fe_2Ti phases. Overall, these XRD results demonstrate the evolution and stabilization of various intermetallic phases as a function of sintering temperature, highlighting the critical role of thermal treatment in tailoring the microstructure and phase composition of Fe-Al-Ti alloys.

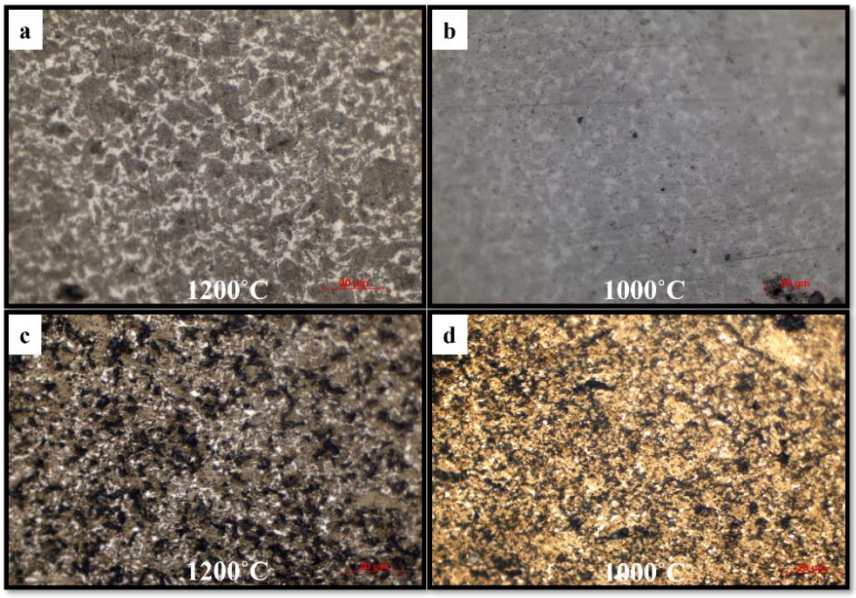

Figure 4.9 Optical image conforming different phase formation of the sintered sample of $Fe_{83.453}Al_{14.560}Ti_{1.987}$ and $Fe_{69.815}Al_{26.860}Ti_{3.325}$ at different sintering temperatures.

Figure 4.9 shows the optical micrographs of the sintered $Fe_{83.453}Al_{14.560}Ti_{1.987}$ [Figures 4.9(a) and 4.9(b)] and $Fe_{69.815}Al_{26.860}Ti_{3.325}$ [Figures 4.9(c) and 4.9(d)] samples after etching. The specimens were etched using Keller's reagent, composed of distilled water, hydrofluoric acid (HF), hydrochloric acid (HCl), and nitric acid (HNO_3). The optical images distinctly reveal the formation of different microstructural phases in the sintered samples.

For both compositions, etching clearly delineates phase contrast and grain boundaries, suggesting successful densification and intermetallic phase development during sintering. The sample sintered at 1200 °C [Figures 4.9(a) and 4.9(c)] displays more distinct and heterogeneous microstructural features compared to those sintered at 1000 °C [Figures 4.9(b) and 4.9(d)], indicating more extensive diffusion and phase transformation at higher temperatures. These observations support the XRD findings and further confirm the evolution of complex phases with increasing sintering temperature.

4.9 SEM Analysis of Sintered Samples and Inter-Particle Bonding

Figures 4.10(a–d) and 4.10(e–h) display the SEM micrographs of $Fe_{83.453}Al_{14.560}Ti_{1.987}$ and $Fe_{69.815}Al_{26.860}Ti_{3.325}$ powders, respectively, after SPS

at various temperatures. These images reveal the progression of inter-particle bonding and microstructural evolution with increasing sintering temperature. At 300 °C [Figure 4.10(a)] and 350 °C [Figure 4.10(e)], both compositions show loosely packed and poorly bonded particles, retaining much of their original powder morphology with noticeable pores and voids. The neck formation between particles is minimal, indicating insufficient atomic diffusion at these low temperatures.

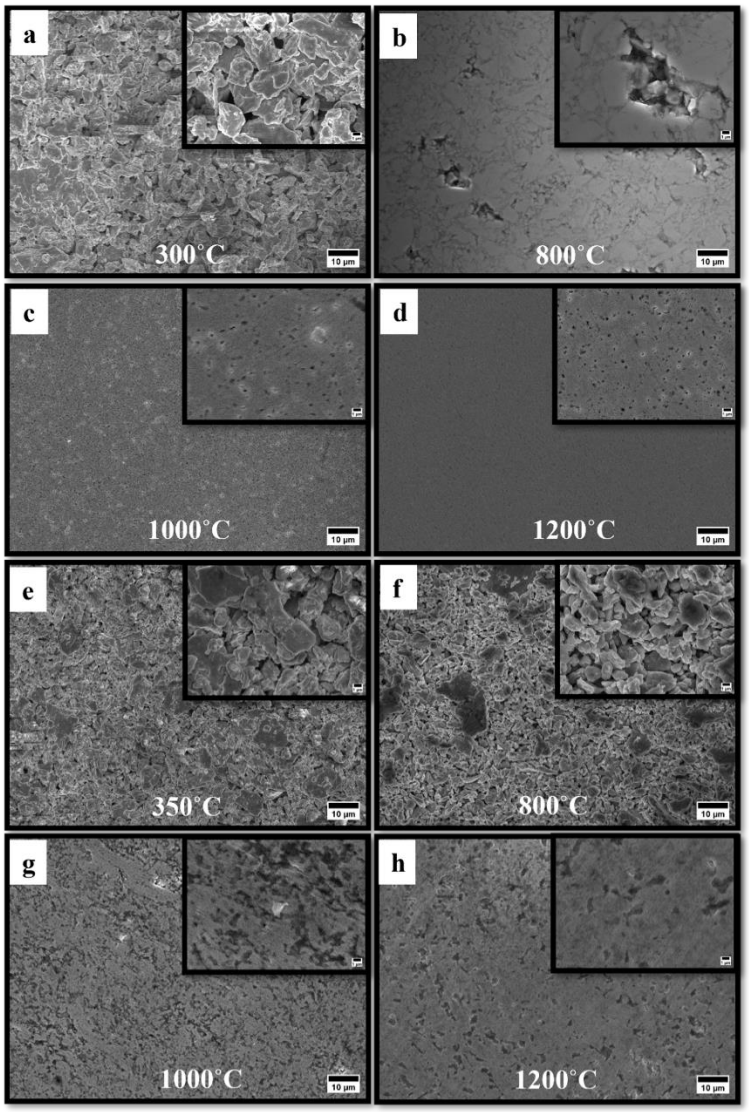

Figure 4.10 Effect of Sintering Temperature on Inter-Particle Bonding in Sintered samples

At 800 °C [Figures 4.10(b) and 4.10(f)], partial sintering is evident. The particles show signs of bonding and neck growth, but the microstructure remains porous, and discrete particle boundaries are still visible. By 1000 °C [Figures 4.10(c) and 4.10(g)], the samples exhibit improved densification, with

smoother surfaces and reduced pore volume. Inter-particle boundaries begin to fade, suggesting significant diffusion-driven consolidation. At the highest sintering temperature of 1200 °C [Figures 4.10(d) and 4.10(h)], both compositions show a dense and relatively pore-free microstructure, with a continuous matrix indicating strong inter-particle bonding and near-complete consolidation.

Overall, the SEM analysis clearly demonstrates that increased sintering temperature enhances densification by promoting solid-state diffusion, neck growth, and elimination of porosity. The improvements are more pronounced in the $Fe_{83.453}Al_{14.560}Ti_{1.987}$ composition, which appears to achieve better particle coalescence and surface uniformity consistent with its higher practical density and lower porosity as discussed earlier.

4.10 Mechanical Properties

4.10.1 Vickers Hardness Test

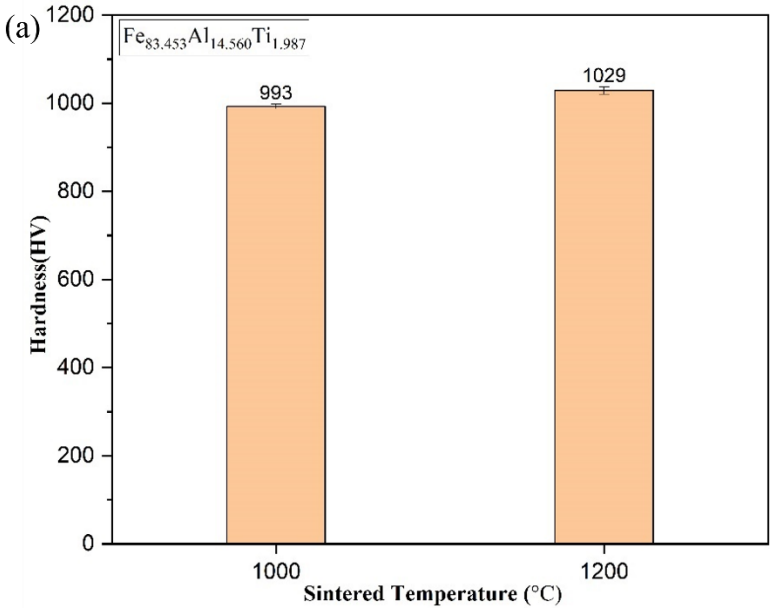

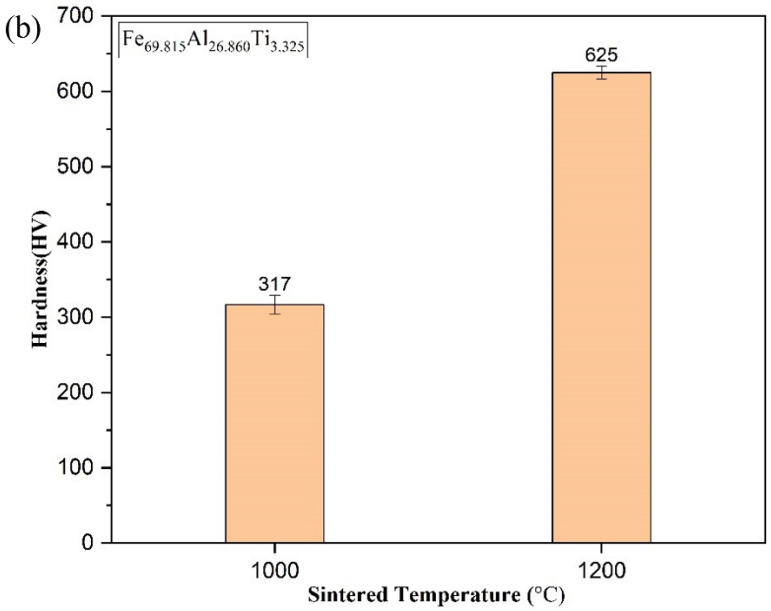

Figure 4.11 Hardness value of both sintered sample at 1000 °C and 1200 °C

Figures 4.11(a) and (b) present the Vickers hardness results for the $Fe_{83.453}Al_{14.560}Ti_{1.987}$ and $Fe_{69.815}Al_{26.860}Ti_{3.325}$ samples, respectively, sintered at 1000 °C and 1200 °C. In Figure 4.11 (a), the Fe-rich composition shows a high hardness value of 993 HV at 1000 °C, which further increases to 1029 ± 8.67 HV at 1200 °C, indicating enhanced densification and likely the formation of fine intermetallic phases at higher temperatures. In contrast, Figure 4.11 (b) shows that the Al- and Ti-rich composition exhibits a lower hardness of 317 HV at 1000 °C, rising to 625 ± 3.97 HV at 1200 °C. The comparatively lower hardness in this composition can be attributed to a higher proportion of low-hardness phases or microstructural porosity. Missing data points at lower temperatures for both samples because of loosely compaction, and the results highlight the crucial role of temperature and composition in determining the mechanical properties of these alloys.

Chapter 5

Conclusion and Future Scope

5.1 Conclusion

The present study focused on synthesis, consolidation and characterization of Fe-based ternary alloys $Fe_{83.453}Al_{14.560}Ti_{1.987}$ and $Fe_{69.815}Al_{26.860}Ti_{3.325}$ produced via Ma and subsequently consolidated using SPS the following key conclusions.

- Mechanical alloying up to 80 hours successfully produced partially to predominantly amorphous structures in both $Fe_{83.453}Al_{14.560}Ti_{1.987}$ and $Fe_{69.815}Al_{26.860}Ti_{3.325}$ compositions. The $Fe_{83.453}Al_{14.560}Ti_{1.987}$ composition showed better glass-forming ability.
- XRD, TEM, and SAED confirmed the presence of amorphous and nanocrystalline phases. SEM-EDS analysis demonstrated improved compositional homogeneity and particle refinement with increased milling time.
- The average particle size reduced significantly during early milling stages and showed slight agglomeration at extended durations due to cold welding. The final particle sizes of $Fe_{83.453}Al_{14.560}Ti_{1.987}$ is 3.57 ± 0.41 μm and $Fe_{69.815}Al_{26.860}Ti_{3.325}$ is 5.17 ± 1.81 μm.

- SPS consolidation at 300–1200 °C enhanced densification and inter-particle bonding. $Fe_{83.453}Al_{14.560}Ti_{1.987}$ consistently showed higher practical density and lower porosity at all sintering temperatures.
- XRD of sintered samples revealed the formation of complex intermetallic phases at elevated temperatures, indicating thermally induced phase evolution.
- Vickers' hardness increased with sintering temperature. The highest hardness 1029 ± 8.7 HV was achieved by the $Fe_{83.453}Al_{14.560}Ti_{1.987}$ sample sintered at 1200 °C, attributed to its superior densification and uniform microstructure.

5.2 Future Scope

1. Explore different compositions of Fe-Al-Ti alloys, and potentially include other elements, to improve their glass-forming ability and mechanical properties.
2. Systematically adjust SPS parameters like heating rate, holding time, and pressure to achieve better densification while keeping the amorphous structure.
3. Investigate how well these optimized Fe-Al-Ti resist corrosion and wear, which is crucial for their use in tough environments.

Additional information

Funding

Financial support from the Council of Scientific & Industrial Research (Sanction lett. No. 22 (O842)/20/EMR-II) is gratefully acknowledged.

References

[1] B. Nair and B. G. Priyadarshini, “Process, structure, property and applications of metallic glasses,” 2016, *AIMS Press*. doi: 10.3934/matersci.2016.3.1022.

[2] L. Yan, B. Yan, and Y. Jian, “Fabrication of Fe-Si-B Based Amorphous Powder Cores by Spark Plasma Sintered and Their Magnetic Properties,” *Materials*, vol. 15, no. 4, Feb. 2022, doi: 10.3390/ma15041603.

[3] M. G. Ozden and N. A. Morley, “Laser additive manufacturing of Fe-based magnetic amorphous alloys,” Feb. 01, 2021, *MDPI AG*. doi: 10.3390/magnetochemistry7020020.

[4] E. A. Olevsky, S. Kandukuri, and L. Froyen, “Consolidation enhancement in spark-plasma sintering: Impact of high heating rates,” *J Appl Phys*, vol. 102, no. 11, 2007, doi: 10.1063/1.2822189.

[5] M. S. Bakare, ; K T Voisey, ; K Chokethawai, and ; D G Mccartney, “Corrosion Behaviour of Crystalline and Amorphous Forms of the Glass Forming Alloy Fe 43 Cr 16 Mo 16 C 15 B 10.”

[6] Q. W. Xing and Y. Zhang, “Amorphous phase formation rules in high-entropy alloys,” *Chinese Physics B*, vol. 26, no. 1, Jan. 2017, doi: 10.1088/1674-1056/26/1/018104.

[7] Z. Feng, H. Geng, Y. Zhuang, and P. Li, “Progress, Applications, and Challenges of Amorphous Alloys: A Critical Review,” *Inorganics (Basel)*, vol. 12, no. 9, p. 232, Aug. 2024, doi: 10.3390/inorganics12090232.

[8] C. Suryanarayana, “Mechanical Alloying: A Novel Technique to Synthesize Advanced Materials,” *Research*, vol. 2019, Jan. 2019, doi: 10.34133/2019/4219812.

[9] T. Fukunaga, K. Nakamura, K. Suzuki, and U. Mizutani, “Amorphization of immiscible Cu□Ta system by mechanical alloying and its structure observation,” *J Non Cryst Solids*, vol. 117–118, no. PART 2, pp. 700–703, Feb. 1990, doi: 10.1016/0022-3093(90)90625-V.

[10] N. Al-Aqeeli, M. A. Hussein, and C. Suryanarayana, “Phase evolution during high energy ball milling of immiscible Nb–Zr alloys,” *Advanced Powder Technology*, vol. 26, no. 2, pp. 385–391, Mar. 2015, doi: 10.1016/J.APT.2014.11.008.

[11] S. Çam, V. Demir, and D. Özyürek, “Wear behaviour of A356/TiAl3 in situ composites produced by mechanical alloying,” *Metals (Basel)*, vol. 6, no. 2, Feb. 2016, doi: 10.3390/met6020034.

[12] M. Radune, M. Zinigrad, and N. Frage, “Optimization of High Energy Ball Milling Parameters for Synthesis of Ti_{1-x}Al_xN Powder,” *Journal of Nano Research*, vol. 38, pp. 107–113, Jan. 2016, doi: 10.4028/www.scientific.net/JNanoR.38.107.

[13] O. Dezellus, B. Gardiola, and J. Andrieux, “On the solubility of group IV elements (Ti, Zr, Hf) in liquid aluminum below 800°C,” *J Phase Equilibria Diffus*, vol. 35, no. 2, pp. 120–126, 2014, doi: 10.1007/s11669-013-0278-2.

[14] V. Mamedov, “Spark plasma sintering as advanced PM sintering method,” *Powder Metallurgy*, vol. 45, no. 4, pp. 322–328, 2002, doi: 10.1179/003258902225007041.

[15] A. Aliouat, G. Antou, N. Pradeilles, V. Rat, and A. Maître, “Investigation of consolidation mechanisms induced by applied electric/electromagnetic fields during the early stages of spark plasma sintering,” *J Alloys Compd*, vol. 963, p. 171276, Nov. 2023, doi: 10.1016/J.JALLCOM.2023.171276.

[16] X. Song, X. Liu, and J. Zhang, “Neck formation and self-adjusting mechanism of neck growth of conducting powders in spark plasma sintering,” *Journal of the American Ceramic Society*, vol. 89, no. 2, pp. 494–500, Feb. 2006, doi: 10.1111/j.1551-2916.2005.00777.x.

[17] J. E. Garay, “Current-activated, pressure-assisted densification of materials,” *Annu Rev Mater Res*, vol. 40, pp. 445–468, 2010, doi: 10.1146/annurev-matsci-070909-104433.

[18] Z. A. Munir, U. Anselmi-Tamburini, and M. Ohyanagi, “The effect of electric field and pressure on the synthesis and consolidation of materials: A review of the spark plasma sintering method,” Feb. 2006. doi: 10.1007/s10853-006-6555-2.

[19] M. Eriksson, Z. Shen, and M. Nygren, “Fast densification and deformation of titanium powder,” *Powder Metallurgy*, vol. 48, no. 3, pp. 231–236, Sep. 2005, doi: 10.1179/174329005X71939.

[20] M. Kwiatkowska, D. Zasada, J. Bystrzycki, and M. Polański, “Synthesis of Fe-Al-Ti based intermetallics with the use of laser engineered net shaping (LENS),” *Materials*, vol. 8, no. 5, pp. 2311–2331, 2015, doi: 10.3390/ma8052311.

[21] Z. Huo, G. Zhang, J. Han, J. Wang, S. Ma, and H. Wang, “A Review of the Preparation, Machining Performance, and Application of Fe-Based Amorphous Alloys,” Jun. 01, 2022, *MDPI*. doi: 10.3390/pr10061203.

[22] X. jie Yuan *et al.*, “A review of the preparation and prospects of amorphous alloys by mechanical alloying,” *Journal of Materials Research and Technology*, vol. 33, pp. 3117–3143, Nov. 2024, doi: 10.1016/j.jmrt.2024.10.026.

[23] L. Sang and Y. Xu, “Amorphous behavior of ZrxFeNiSi0.4B0.6 high entropy alloys synthesized by mechanical alloying,” *J Non Cryst Solids*, vol. 530, Feb. 2020, doi: 10.1016/j.jnoncrysol.2019.119854.

[24] L. Zhang and H. Huang, “Micro machining of bulk metallic glasses: a review,” Jan. 16, 2019, *Springer London*. doi: 10.1007/s00170-018-2726-y.

[25] D. W. Zhang *et al.*, “Magnetic properties evaluation of Fe-based amorphous alloys synthesized via spark plasma sintering,” *J Non Cryst Solids*, vol. 613, Aug. 2023, doi: 10.1016/j.jnoncrysol.2023.122373.

[26] X. Qi *et al.*, “A Review of Fe-Based Amorphous and Nanocrystalline Alloys: Preparations, Applications, and Effects of Alloying Elements,” Jul. 01, 2023, *John Wiley and Sons Inc*. doi: 10.1002/pssa.202300079.

[27] A. V. Nosenko *et al.*, “Soft magnetic cobalt based amorphous alloys with low saturation induction,” *J Magn Magn Mater*, vol. 515, Dec. 2020, doi: 10.1016/j.jmmm.2020.167328.